Resonance-enhanced magnetic X-ray diffraction from a rare-earth alloy

1994 J. Phys.: Condens. Matter 6 2409

(http://iopscience.iop.org/0953-8984/6/12/016)

J. Phys.: Condens. Matter 6 (1994) 2409–2422. Printed in the UK

Resonance-enhanced magnetic x-ray diffraction from a rare-earth alloy

D B Pengra†§, N B Thoft†, M Wulff‡, R Feidenhans'l† and J Bohr†

† Department of Solid State Physics, Risø National Laboratory, DK-4000 Roskilde, Denmark

‡ European Synchrotron Radiation Facility, 38043 Grenoble Cédex, France

Received 5 August 1993

Abstract. A single crystal of a rare-earth random-site alloy, $Ho_{0.5}Er_{0.5}$, has been studied with x-ray diffraction. We have used the technique of resonance-enhanced scattering at the Ho and Er L_{III} absorption edges to study element-specific effects in the temperature dependence of the magnetic structure below the Néel temperature. In the highest-temperature phase, a *c*-axis modulated structure in which the Ho and Er moments take different tilt angles from the basal plane, measurements at the two edges show identical satellite positions. The lowest-temperature phase, a conical spiral which locks to a structure with wavevector $\frac{2}{40}c^*$ below 20 K, is accompanied by a basal-plane lattice modulation that is related to the magnetic structure. The modulation changes the symmetry of the crystal lattice; as a consequence we suggest that the magnetic structure locks to one with equidistant spin-slip discommensurations. In addition, we find an unusual energy and polarization dependence in the satellite intensity in this phase that is not seen at higher temperatures. We present arguments to demonstrate that the unusual behaviour is not accounted for by multiple-scattering events.

1. Introduction

1.1. The magnetic phases of Ho, Er and $Ho_{0.5}Er_{0.5}$

Crystals of the rare-earth metals holmium and erbium are remarkable in that their chemical and physical properties are similar, but their magnetic structures are quite different. The origin of this interesting contrast has been ascribed to the competition between the basic interaction which gives rise to the magnetic structure—the Ruderman–Kittel–Kasuya–Yosida (RKKY) interaction—and the effects of the crystal field [1–3]. The RKKY model treats the rare-earth crystal as a system of localized magnetic moments embedded in a free-electron gas; the perturbation of the electron gas produces an oscillatory coupling (i.e. varying between ferromagnetic and antiferromagnetic) between individual moments depending on their relative separation. The ground state of the RKKY model is a set of ferromagnetic sheets, coincident with the basal planes of the crystal, which are stacked such that the moment direction from one plane to the next is rotated through a fixed angle determined by the system's minimum energy; such a structure is called a *basal-plane spiral*.

The effects of finite temperature and the crystal field modify the basic spiral structure. In the case of erbium the crystal-field anisotropy favours alignment along the crystal's *c* axis. In general, the effects of the crystal field tend to increase with decreasing temperature, and we find the following sequence of phases, as illustrated in figure 1. At the highest

§ Present address: Department of Physics, Hasbrouck Laboratory, University of Massachusetts, Amherst, MA 01003, USA.

0953-8984/94/122409+14$19.50

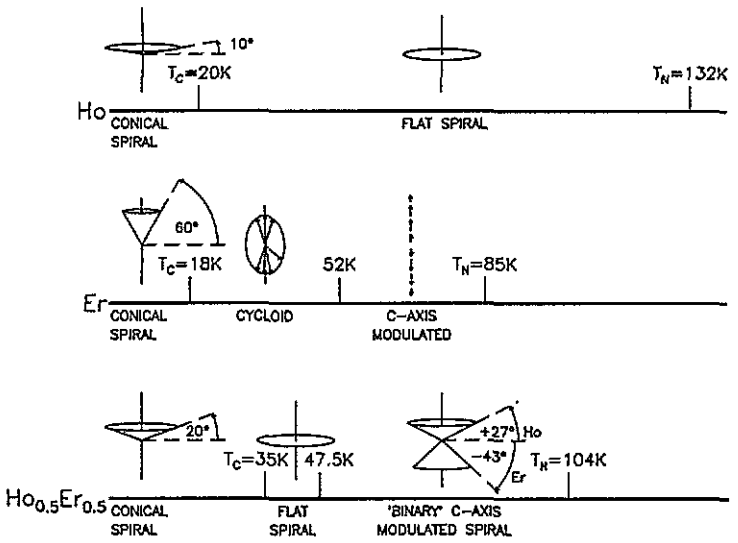

Figure 1. The magnetic phases of Ho, Er and $Ho_{0.5}Er_{0.5}$ as presently understood. See text for discussion.

temperatures, below a Néel point $T_N = 85$ K, there is no ordering of the moments in the basal planes, but rather a *c*-axis modulated structure in which the moment projections on the *c* axis alternate sinusoidally. Below 52 K some basal-plane ordering appears. Early neutron work [4] indicated that the moments ordered along both basal-plane axes. A more recent study, which includes an analysis of a mean-field model whose Hamiltonian includes single-ion anisotropy and anisotropic ion couplings with the RKKY interaction, proposes that the ordering occurs predominantly in one plane [3]. This is a *cycloidal* structure in which the moments in successive planes are rotated as if they lay on an ellipse that was being turned end-over-end perpendicular to the basal planes. Finally, at a Curie temperature $T_C = 18$ K, the *c*-axis modulation vanishes, and the moments form a *conical spiral*: there is a net magnetization along, and a specific turn angle about, the *c* axis; the moments tilt with an angle of $\approx 60°$ with respect to the basal plane [4].

The situation with holmium is quite different and somewhat simpler. Here, the crystal anisotropy favours ordering in the basal plane. Consequently, at higher temperatures, below $T_N = 132$ K, the preferred structure is a basal-plane spiral. There is no intermediate temperature phase as in Er, but at $T_C = 20$ K the spiral tilts out of the plane by about 10° to form a conical spiral [5, 6].

The above picture has been modified in recent years by the discovery of commensurate phases in the antiferromagnetic regions ($T_C < T < T_N$) of both Ho and Er. These phases are indicated in high-resolution diffraction experiments [3, 7–10] which show that the positions of magnetic satellites as a function of temperature proceed through a sequence of values which are given by simple fractions of the basic reciprocal lattice vector. We will return to this issue in section 2, when we discuss the behaviour of the lowest-temperature phase of $Ho_{0.5}Er_{0.5}$.

The very different magnetic structures displayed by otherwise similar materials suggests the question: what would happen upon alloying the two metals? Would the magnetic structures tend to conform to one or other of the forms found in the pure materials, or would there appear entirely new structures not seen in either? Further, is it possible that the Ho and Er moments might order differently, or would they instead behave as a uniform system at all temperatures?

Magnetization measurements on $Ho_{0.5}Er_{0.5}$ show that it has a Curie temperature of 35 K,

as compared to ≈ 20 K in pure Ho and Er. The Néel temperature of the alloy is found to be nearly the average of those of the two constituents, equal to 104 K [2].

The first neutron diffraction experiment [11] on $Ho_{0.5}Er_{0.5}$ indicated that the low-temperature ferrimagnetic phase was a conical spiral (as in pure Ho and Er) with the tilt angle of the cone from the basal plane equal to 37° (at 4 K), which is intermediate between the angles for the pure metals. Above T_C this study found that the structure became a simple basal-plane spiral whose average turn angle increased continuously from 41.8° at the transition to 50.7° at T_N.

A recent neutron diffraction study [12] performed on the same sample as the present x-ray study confirmed the finding that the lowest-temperature structure was a conical spiral with a tilt angle of $\approx 20°$ with respect to the basal plane (at 10 K). The data were fit to a model in which the moments of the two elements were allowed to take different tilt angles, but the best fit was to a structure in which the tilt angles were the same for both Ho and Er; it appeared that the different moments behaved as a uniform system in this temperature range. This study also found that the structure transformed to a uniform basal-plane spiral at T_C, as reported earlier; yet this phase gave way to another phase at 43 K which had not been seen before. Again, allowing the tilt angles to vary, the best fit in this temperature range was for a *binary* phase: a model that could be described as a c-axis modulated spiral, in which each of the Ho and Er moments takes a different tilt angle with respect to the basal plane. The fitting gave a tilt angle of +27° for the Ho moments and −43° for the Er moments. These numbers come from holding the total moment μ equal to that determined for the intermediate-temperature spiral phase ($10.3\,\mu_B$) and fitting the data taken just above the transition at 50 K. The tilt-angle values were sensitive to the value of μ; a reduction by 5% gave +23° and −38° for the Ho and Er moments respectively.

1.2. Resonance-enhanced magnetic x-ray scattering

The possibility of binary magnetic phases—a separate ordering of the moments of the two elements in the alloy—is one of the motivations behind the present x-ray study. In the technique of *resonance exchange scattering* [13, 14] one tunes the incident radiation to an absorption edge in the sample. Under the proper conditions this brings into play a resonance which is related to the magnetic structure, and which substantially enhances the scattering cross section. As the energy of the resonance is strongly element-dependent, the technique allows one to study the magnetic ordering of different elements separately.

The theory of magnetic photon scattering has been described recently by many authors [13, 15–20]. The elastic scattering cross section from a single crystal has the form [18, 21]

$$\frac{d\sigma}{d\Omega} = \left(\frac{e^2}{mc^2}\right)^2 \left| \sum_n^{\text{all atoms}} e^{iQ\cdot r_n} f_n(k, k'; \hbar\omega) \right|^2 \tag{1}$$

where m and e are the mass and charge of an electron, r_n are the vectors giving the positions of the atoms, $Q = k - k'$ is the photon momentum transfer, and $\hbar\omega$ is the photon energy.

If the incident x-rays are tuned to an absorption edge anomalous contributions to the scattering amplitude $f_n(k, k'; \hbar\omega)$ become important. In the special case that the spin–orbit interaction is strong and there is a significant splitting in the valence-band states resulting in the creation of spin-up and spin-down bands, the anomalous scattering amplitude $f' + if''$ can give information about the magnetic state of the system [13, 22]. In the case of the L edges of the rare earths the magnetic structure is reflected in electric dipole (E1) resonances

involving 2p ↔ 5d transitions and electric quadrupole (E2) resonances involving 2p ↔ 4f transitions.

In most of what follows we take $f_n(k, k'; \hbar\omega)$ to be dominated by the E1 resonant contribution; this is reasonable when the incident radiation is tuned to this resonance, and one is using a polarization analyser to measure the intensity of satellites arising from antiferromagnetic ordering. Within certain approximations, this contribution may be written in the convenient form [13]:

$$f_{n\,\mathrm{E1}}^{(\mathrm{xres})} = \tfrac{3}{4}\mathrm{i}[\hat{e}' \cdot \hat{e}(F_{11} + F_{1-1}) - \mathrm{i}(\hat{e}' \times \hat{e}) \cdot \hat{z}_n(F_{11} - F_{1-1}) + (\hat{e}' \cdot \hat{z}_n)(\hat{e} \cdot \hat{z}_n)(2F_{10} - F_{11} - F_{1-1})] \tag{2}$$

where $\hat{e}$ ($\hat{e}'$) gives the incident (scattered) polarization and $\hat{z}_n$ gives the orientation of the magnetic moment of the nth ion. The F_{LM} depend strongly on energy and represent the various strengths of different resonant transitions [13, 23]. That $F_{11} \neq F_{1-1}$ allows the resonant amplitude to reflect the magnetic state of the crystal. The first term in (2) will contribute only to the Bragg peaks as it does not depend on $\hat{z}_n$. For a basal-plane spiral antiferromagnet measured along the [001] direction the second term will contribute to first-order satellites, and the third term, being quadratic in $\hat{z}_n$, will contribute to the Bragg peaks and second-order satellites.

Synchrotron light is highly linearly polarized, with the electric field vector lying in the plane of the electron orbit. In our experiment the scattering plane is perpendicular to the predominant polarization; by convention we say that the light is incident with σ polarization; light with its polarization parallel to the scattering plane is called π polarized. As indicated by the vector product in the second term of (2), light incident on the sample with σ polarization will scatter from the first-order satellite with π polarization. In contrast, light scattered by the charge of the atoms has its polarization unchanged; i.e. it will scatter $\sigma \rightarrow \sigma$. As most of the background or diffuse scattering is of the charge-scattered type, we may use a polarization filter to both separate the 'magnetic' ($\sigma \rightarrow \pi$) peaks from the charge-scattered peaks and to greatly reduce the background in the measurement of the magnetic structure.

The polarization analysis is accomplished by diffracting the scattered light through approximately 90° [24]. For Ho-edge measurements at 8069 eV this is approximately satisfied by the (006) reflection graphite, and for the Er-edge measurements at 8358 eV we used the (222) reflection from a Cu crystal.

Following Blume and Gibbs [18], we find it useful to write the polarization dependence in (2) in terms of an experimentally relevant basis, namely the directions of the incident and scattered beam $\hat{k}$ and $\hat{k}'$, and a direction perpendicular to these $(\hat{k}' \times \hat{k})/\sqrt{1 - (\hat{k} \cdot \hat{k}')^2}$. We represent the scattering amplitude in terms of a two-by-two matrix $\mathcal{M}$ in these quantities which takes light incident with polarization $|\epsilon_\sigma\rangle\,\hat{e}_\sigma + |\epsilon_\pi\rangle\,\hat{e}_\pi$ to $|\epsilon'_\sigma\rangle\,\hat{e}'_\sigma + |\epsilon'_\pi\rangle\,\hat{e}'_\pi$.

In terms of this matrix the general scattering cross section (1) may be rewritten as

$$\frac{\mathrm{d}\sigma}{\mathrm{d}\Omega} = \left(\frac{e^2}{mc^2}\right)^2 \sum_{\epsilon,\epsilon'} p_\epsilon \left|\langle\epsilon|\,\mathcal{M}\,|\epsilon'\rangle\right|^2 \tag{3}$$

where p_ϵ gives the probability that the light will be incident with a particular state ϵ.

We obtain the resonant E1 contribution to $\mathcal{M}$ as

$$\mathcal{M}_{\mathrm{E1}}^{(\mathrm{xres})} = \sum_{n}^{\text{all atoms}} \mathrm{e}^{\mathrm{i}Q\cdot r_n} \mathcal{M}_{n\,\mathrm{E1}}^{(\mathrm{xres})} \tag{4}$$

where

$$\mathcal{M}_{n\,\mathrm{E1}}^{(\mathrm{xres})} = \begin{pmatrix} 1 & 0 \\ 0 & \hat{k}\cdot\hat{k}' \end{pmatrix} F^{(0)} - \mathrm{i}\begin{pmatrix} 0 & \hat{k}\cdot\hat{z}_n \\ -\hat{k}'\cdot\hat{z}_n & (\hat{k}'\times\hat{k})\cdot\hat{z}_n \end{pmatrix} F^{(1)} + \begin{pmatrix} [(\hat{k}'\times\hat{k})\cdot\hat{z}_n]^2 & [(\hat{k}'\cdot\hat{z}_n) - (\hat{k}'\cdot\hat{k})(\hat{k}\cdot\hat{z}_n)](\hat{k}'\times\hat{k})\cdot\hat{z}_n \\ \left\{\begin{array}{c}[(\hat{k}'\cdot\hat{k})(\hat{k}'\cdot\hat{z}_n) \\ -(\hat{k}\cdot\hat{z}_n)](\hat{k}'\times\hat{k})\cdot\hat{z}_n\end{array}\right\} & \left\{\begin{array}{c}(\hat{k}'\cdot\hat{k})[(\hat{k}\cdot\hat{z}_n)^2 + (\hat{k}'\cdot\hat{z}_n)^2] \\ +[1+(\hat{k}'\cdot\hat{k})^2](\hat{k}'\cdot\hat{z}_n)(\hat{k}\cdot\hat{z}_n)\end{array}\right\} \end{pmatrix} \times \frac{F^{(2)}}{1-(\hat{k}'\cdot\hat{k})^2}$$

with

$$F^{(0)} \equiv \tfrac{3}{4}\pi(F_{11} + F_{1-1}) \qquad F^{(1)} \equiv \tfrac{3}{4}\pi(F_{11} - F_{1-1}) \qquad F^{(2)} \equiv \tfrac{3}{4}\pi(2F_{10} - F_{11} - F_{1-1}).$$

The polarization analyser acts on $|\epsilon'\rangle$ and, depending on its orientation, will pass either $|\epsilon'_\sigma\rangle$ or $|\epsilon'_\pi\rangle$ to the detector. Consequently, in this representation the $\sigma \rightarrow \pi$ intensity is proportional to $|\mathcal{M}_{21}|^2$ and the $\sigma \rightarrow \sigma$ intensity to $|\mathcal{M}_{11}|^2$.

2. Experimental methods and results

2.1. The sample, equipment and calibration

The sample in this study is the same one used in the previously discussed neutron work [12]: it is a single-crystal random-site alloy of 50% holmium and 50% erbium, which has been cut to a rectangular box of $5 \times 3 \times 2.5$ mm such that the [001] direction lies along the long axis of the box. Holmium and erbium have an HCP structure, and the two metals have lattice constants which are similar [25]. The alloy has the same structure, and we find the lattice constants to be intermediate between the two pure materials; our sample has $a, b = 3.567$ Å and $c = 5.625$ Å at $T = 12$ K.

The measurements were made at beamline W1 at the Hamburgersynchrotronstrahlungslabor (HASYLAB) in Germany [26]. The sample was mounted inside a sealed beryllium can containing helium as a heat-transfer medium, which was installed in a Displex closed-cycle helium refrigerator capable of cooling to 12 K. The crystal was oriented on the diffractometer such that the $\{00l\}$ planes of the crystal were in a reflection geometry in the vertical plane, and the [100] direction was in the scattering plane.

Energy calibration was accomplished by tuning the incident radiation through the Ho L_{III} absorption edge and measuring the fluorescence yield with a Ge solid-state counter of energy resolution ≈ 300 eV. The inflection point of the fluorescence intensity against energy was set to 8069 eV.

2.2. Temperature dependence of the resonant satellites

Figure 2 shows the variation in length q of the resonant satellite vector as a function of T measured at both the Ho and Er L_{III} edges in the $\sigma \rightarrow \pi$ polarization channel. These data, taken from the satellite at $(0, 0, 4 + q)$, reproduce the results found in the neutron measurements with $q_{\mathrm{Ho}} = q_{\mathrm{Er}} = q_{\mathrm{neutron}}$ at all temperatures below T_{N}. The regions of the three phases found in the neutron work are marked by the vertical broken lines in the figure.

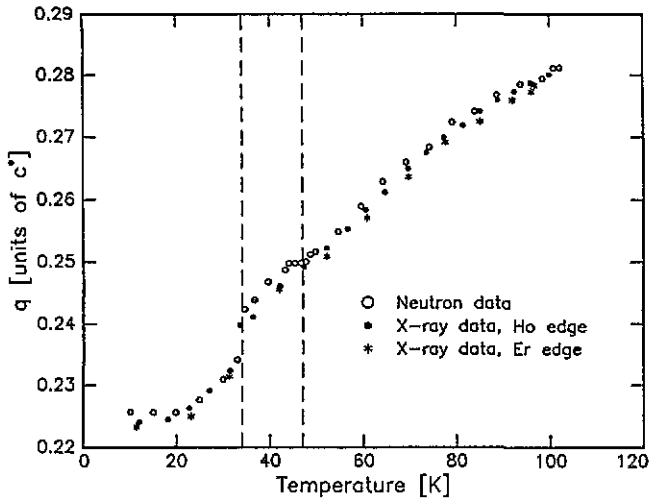

Figure 2. Length of the resonant satellite vector q as a function of temperature. The x-ray data are for the $(0, 0, 4 + q)$ satellite taken at the Ho resonance at 8069 eV (•) and the Er resonance at 8358 eV (*). Also shown are neutron measurements (o) of [12] taken from the $(0, 0, 2 - q)$ satellite. The vertical lines show the boundaries of the three phases found in the neutron study.

At the Curie temperature $T_C = 35$ K one can see an abrupt change in q, which locks-in to a value of $q = 0.225c^*$ at 20 K.

The similarity of the data from the Ho and Er resonances between $T_N = 104$ K and 47 K, the region of the binary phase, indicates that the Er and Ho moments order at the same temperature. With resonant x-ray scattering in the $\sigma \rightarrow \pi$ channel the dominant term in the dipole contribution to the scattering amplitude is proportional to $\hat{k}' \cdot \hat{z}_n$. Consequently, the presence of the $(0, 0, 4 + q)$ satellite can be due to ordering either in the basal plane, or perpendicular to it. This contrasts with the situation for (unpolarized) neutrons, where the scattering amplitude is proportional to $\hat{Q} \times (\hat{z}_n \times \hat{Q})$: for neutron scattering, satellites along the [001] direction are due only to ordering in the basal planes. Yet it is noteworthy that because $q_{Ho} = q_{Er}$ the period of the ordering in this direction is uniform whether the individual moments belong to one element or the other, and whether Er moments orient differently from the Ho moments.

A comparison of integrated intensity for the same set of measurements as in figure 2 shows a somewhat different picture. As shown in figure 3, between 47 K and T_N the Ho- and Er-edge peaks vanish at the same Néel temperature, and the intensity for each decreases approximately linearly as a function of T. This may be compared with the neutron data: above 47 K, the neutron intensity follows a law of the form

$$I^{(\text{neutron})} = A(1 - T/T_N)^{\gamma}$$

where A is a scaling constant and $\gamma = 0.43$ [12]. The nearly linear temperature dependence of the x-ray satellite intensity has also been seen in a study of pure Ho [21]†, and it was reported in this study that within the statistics of the measurement the temperature dependence is the same both on- and off-resonance. More recent work on Ho, however, indicates that both the neutron and resonant x-ray intensities follow a power-law behaviour in temperature with $\gamma \approx 0.8$ [28]. The reasons for the difference between our x-ray results and the earlier neutron results are unclear, but they may depend on the different sensitivities

† The nearly linear decay of the Ho $(0, 0, 2 + q)$ satellite as $T \rightarrow T_N$ is evident on re-plotting the data of figure 17 in [21]. There is also evidence that the intensities of different resonant satellites of Ho have different temperature behaviour: the intensity of the $(0, 0, 2 - q)$, $(0, 0, 2 - 2q)$ and $(0, 0, 2 - 3q)$ satellites follow $(1 - T/T_N)^{2\beta}$ where $2\beta = 0.79$, 1.8 and 3.7, respectively [27].

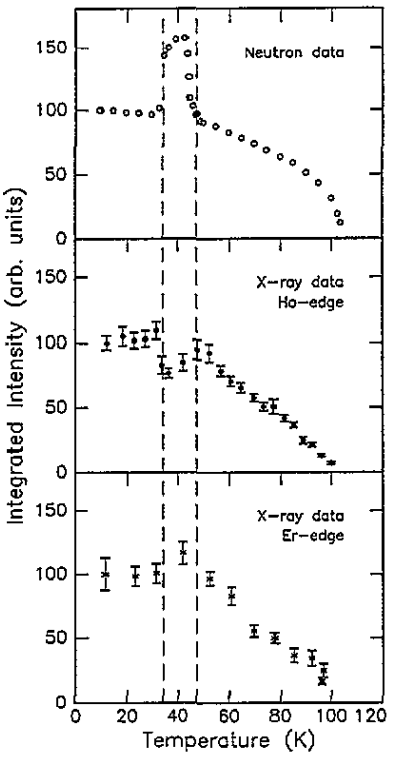

Figure 3. Integrated intensity of the resonant satellites from the same data series as in figure 2: Ho-edge x-ray data (•), Er-edge x-ray data (*), and neutron data (o). The vertical lines mark the boundaries of the three magnetic phases.

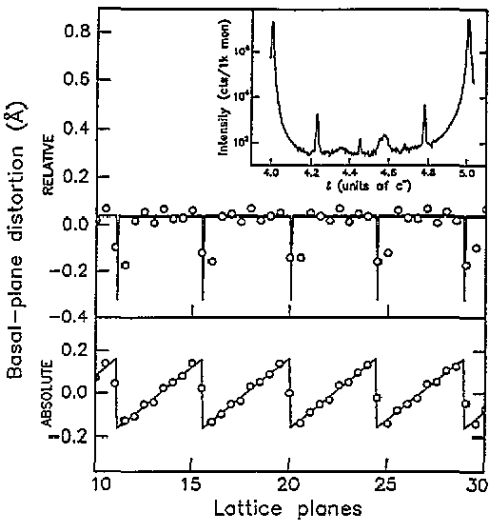

Figure 4. Schematic of the transverse lattice distortion derived from a fit of (8) to the charge-scattered satellites along the [10*l*] line shown in the inset. (The $(1, 0, 5-2K)$ and $(1, 0, 5-3K)$ satellites are partly obscured by powder peaks.) The circles show the lattice-plane displacement from the equilibrium position projected on the [100] direction calculated from a fit to three orders of satellites. The full lines give the displacement due to a sawtooth wave of the same amplitude.

of the cross sections to the moment orientations, or on the much smaller penetration of x rays in comparison with neutrons, which makes them more sensitive to surface effects such as surface-mediated ordering.

A more striking disparity between the neutron and x-ray data is seen in the measurements from the intermediate-temperature phase between 35 K and 47 K. Compared to the measurements in the lowest-temperature phase, we see a significant decrease in the Ho-resonance intensity whereas the neutron intensity increases. This behaviour may be qualitatively understood by a closer examination of the resonant x-ray cross section. In the $\sigma \rightarrow \pi$ channel the E1 contribution to the resonant amplitude (4) of the first-order satellite is

$$f_{n\,\mathrm{E1}}^{(\mathrm{xres})}(\sigma \rightarrow \pi) = \mathrm{i}\hat{\boldsymbol{k}}' \cdot \hat{\boldsymbol{z}}_n F^{(1)} + \left(\frac{[(\hat{\boldsymbol{k}}' \cdot \hat{\boldsymbol{k}})(\hat{\boldsymbol{k}}' \cdot \hat{\boldsymbol{z}}_n) - (\hat{\boldsymbol{k}} \cdot \hat{\boldsymbol{z}}_n)](\hat{\boldsymbol{k}}' \times \hat{\boldsymbol{k}}) \cdot \hat{\boldsymbol{z}}_n}{1 - (\hat{\boldsymbol{k}}' \cdot \hat{\boldsymbol{k}})^2} \right) F^{(2)}. \tag{5}$$

The lowest-temperature phase is a conical spiral; in this phase $\hat{\boldsymbol{z}}_n$ may be parametrized by the vector $(\sin\alpha\cos(\boldsymbol{q}\cdot\boldsymbol{r}_n), \sin\alpha\sin(\boldsymbol{q}\cdot\boldsymbol{r}_n), \cos\alpha)$, where α is the half-cone angle. For scans along the [001] direction we may let $\hat{\boldsymbol{k}} = (\cos\theta, 0, \sin\theta)$ and $\hat{\boldsymbol{k}}' = (\cos\theta, 0, -\sin\theta)$.

In the approximation that the scattering cross section is entirely due to (5) we obtain

$$\left(\frac{d\sigma}{d\Omega}\right)_{E1}^{\sigma\to\pi} = \left(\frac{e^2}{mc^2}\right)^2 \left| \sum_n^{\text{all atoms}} e^{iQ\cdot r_n} \left(\sin\theta\cos\alpha F^{(1)} + \frac{\cos\theta\sin\alpha}{2}(F^{(1)} \pm \cos\alpha F^{(2)})e^{\pm iq\cdot r_n} \pm \frac{\sin\theta\sin^2\alpha}{4} F^{(2)} e^{\pm i2q\cdot r_n} \right) \right|^2. \quad (6)$$

Depending on the half-cone angle α and the sign and magnitude of $F^{(2)}$ the intensity of first-order satellites may increase or decrease with a change in α; for the $(0, 0, k-q)$ satellite the maximum intensity occurs when $\cos\alpha/\cos 2\alpha = -F^{(2)}/F^{(1)}$. For neutron scattering, however, the maximum intensity occurs when Q is perpendicular to the moment orientation, which would be when $\cos\alpha = 0$. Hence, in the transition from the conical-spiral phase to the basal-plane spiral phase the neutron intensity of this satellite will increase, but the resonant x-ray intensity may increase or decrease if the magnitude of $F^{(2)}/F^{(1)}$ is sufficiently large.

We may estimate the ratio $F^{(2)}/F^{(1)}$ from published data with the help of (6) and the equivalent expression for the cross section for the E1 $\sigma \to \sigma$ channel. In pure Ho between T_C and T_N there is a basal-plane spiral: $\alpha = 90°$. Consequently, the satellite intensity measured at the E1 resonance energy is largely due to $F^{(1)}$ at the first-order position and due to $F^{(2)}$ at the second-order position. From figure 7 of [21] we take $I(0, 0, 2+q)/I(0, 0, 2+2q) \approx 25$. This gives $F^{(1)} \approx 2.8F^{(2)}$, from which it follows that the maximum intensity would occur at $\alpha = 73°$, or at an angle from the basal plane of about 17°, which is close to the neutron-measured angle of $\approx 20°$ [12]. The actual change in intensity at the phase transition will depend on the number of moments tilted positively from the basal planes against the number tilted negatively; i.e. it will depend on the structure of the magnetic domains below T_C.

Finally, we note that if $F^{(2)}/F^{(1)}$ for Er has the opposite sign of that for Ho it may explain the apparent increase in the Er-edge satellite intensity in the mid-temperature basal-plane spiral phase, which contrasts with the Ho-edge behaviour.

2.3. The lowest-temperature phase

2.3.1. Basal-plane lattice modulation. With the sample cooled to 12 K and the incident energy tuned to 8040 eV (27 eV below the Ho L_{III}-resonance) a scan along the [10l] line shows that the lowest-temperature phase is accompanied by a lattice modulation. This is indicated by the existence of non-resonant, or 'charge', satellites along this line, as is shown in figure 4. The charge peaks are absent (or nearly absent) in a scan along the specular [00l] line; only weaker non-resonant magnetic peaks are found here which also scatter $\sigma \to \pi$ [18]. The absence of charge satellites along the [00l] line indicates that the lattice modulation is transverse to the basal planes, as a scan along this direction probes only the c-axis order. The lattice-distortion satellites vanish when the crystal is warmed to 40 K, but the much weaker magnetic peaks along the [00l] line remain.

We model the diffraction due to a lattice modulation as follows. We let the atomic vectors $\{r_n\}$ in (1) be given by lattice vectors of the undistorted lattice $\{R_n\}$, which are modulated by a wave represented by a Fourier sine series:

$$r_n = R_n + A\sum_j a_j \sin(jK\cdot R_n). \quad (7)$$

The a_j are the Fourier coefficients, $\boldsymbol{A}$ is a vector parallel to the crystal basal planes which gives the polarization and overall amplitude of the distortion wave, and $\boldsymbol{K}$ is the distortion propagation wavevector perpendicular to $\boldsymbol{A}$.

The expression for the cross section (1) becomes

$$\frac{\mathrm{d}\sigma}{\mathrm{d}\Omega} = \left(\frac{e^2}{mc^2}\right)^2 \left| \sum_n^{\text{all atoms}} f_n \exp\left[i\boldsymbol{Q} \cdot \left(\boldsymbol{R}_n + \boldsymbol{A} \sum_j a_j \sin(j\boldsymbol{K} \cdot \boldsymbol{R}_n) \right) \right] \right|^2$$

$$= \left(\frac{e^2}{mc^2}\right)^2 \left| \sum_n^{\text{all atoms}} \sum_{m_1, m_2, \ldots, m_j, \ldots} f_n \prod_j J_{m_j}(a_j \boldsymbol{A} \cdot \boldsymbol{Q}) e^{i(\boldsymbol{Q} + m_j j\boldsymbol{K}) \cdot \boldsymbol{R}_n} \right|^2 \tag{8}$$

where we have used an identity from the theory of Bessel functions [29]:

$$e^{ix \sin\phi} = \sum_{m=-\infty}^{\infty} J_m(x) e^{im\phi}. \tag{9}$$

Off resonance, the anomalous contributions to the form factor f_n may be neglected; it depends largely on the charge density alone. Thus, the modulation produces charge satellites located at $\boldsymbol{Q} = \boldsymbol{G} - jm_j\boldsymbol{K}$ ($j, m_j = 0, \pm 1, \pm 2, \ldots$). We fit (8) to the integrated intensity of the modulation satellites shown in the inset of figure 4. As we see at most three orders of charge satellites in the data, we truncate the Fourier series in (7) to three terms. The fit gives $\boldsymbol{A} \cdot \boldsymbol{a}^* = 0.21$, $a_1 = +1$ (fixed), $a_2 = -0.43$ and $a_3 = +0.30$, with estimated errors on a_2 of 10% and a_3 of 30%. We thus find that the values of a_n correspond well to what would be generated by a right-triangular, or 'sawtooth', wave: $a_1 = +1, a_2 = -1/2, a_3 = +1/3$. The overall strain amplitude in the [100] direction is 0.32 Å. We also find by a separate fit of the satellites to a Lorentzian lineshape that $|\boldsymbol{K}| = 0.225\boldsymbol{c}^*$, which is identical to $|\boldsymbol{q}|$ of the magnetic structure. In terms of the real space lattice this type of distortion produces a constant strain of ≈ 0.03 Å between successive lattice basal-planes, which is interrupted every 8–9 lattice planes by a slip of ≈ 0.3 Å. This is depicted schematically in figure 4.

We may relate the lattice distortion to the magnetic structure in two ways. First, the distortion is apparently due to the stresses arising from the magnetic structure, as the distortion possesses the same symmetry. The magnetic structure is such that the basal planes are ferromagnetic sheets, but the moment orientation changes from one sheet to the next; consequently a distortion induced by the magnetism should not give rise to a buckling of the basal planes, as the force perpendicular to the sheets should be everywhere the same. Second, when the lattice slips are introduced, the sixfold symmetry of the HCP lattice is reduced. The change in symmetry allows a commensurate structure to form, which was inhibited in the lattice with higher symmetry. This may be understood through the theory of spin-slips [9], which we reiterate as follows.

Consider a simple spiral structure with wavevector length q_m. Between one atomic plane and the next the local moment advances by a phase $2\pi q_m/\tau$, where τ is the length of the wavevector corresponding to the interplanar separation; for an HCP lattice $\tau = 2c^*$. Now, we impose another structure on the system—the crystal field—and consider its symmetry as it affects the magnetic structure. For the spiral with the moments lying in the basal planes the symmetry of the HCP lattice is sixfold; hence, the crystal field introduces a perturbation of the phase parameter with a sixfold degeneracy. In general, the perturbation may be f-fold degenerate, and we consider the progression of the moments through a field which has a period $2\pi/f$. Let the phase parameter of one plane lie in such a period; then in the next plane the phase will have advanced to lie in the next period or not. In other words, it is

self-evident that there is some integer $k \geqslant 1$ such that $2\pi q_m(k-1)/\tau \leqslant 2\pi/f \leqslant 2\pi q_m k/\tau$. The k which satisfies this relation is the smallest integer which satisfies

$$kf \geqslant \tau/q_m. \tag{10}$$

The magnetic structure may be conceived as a sequence of blocks of lengths k and $k-1$. *Whenever there is a block of length $k-1$, we say that there is a spin slip in the structure.* The definition connotes the condition that the moments relax under the influence of the perturbing potential: there is a greater advance in the phase parameter between a block of length $k-1$ and a block of length k than between two blocks of length k. In terms of the perturbing potential the average phase advances $2\pi/fk$ per layer, but the average phase advance between layers with a spin slip is twice this amount. We find the average number of atomic layers between spin slips x_s by equating the phase advance due to the unperturbed structure $2\pi x_s q_m/\tau$ to the phase advance due to the perturbing potential with one spin slip $2\pi(x_s+1)/kf$:

$$x_s = 1/(q_m kf/\tau - 1). \tag{11}$$

A simple commensurate structure has $x_s = \infty$, as all blocks have length k. If $[x_s - (k-1)]/k = p$, where p is an integer, the sequence of blocks may repeat in a regular fashion described by the notation $\cdot p$, where the dot signifies a block of length $k-1$ and p denotes the number of blocks of length k. In this case the two competing periodicities are *commensurate* and the spin-slips equidistant. If x_s itself is not an integer, then the sequence of k and $k-1$ either makes a yet higher-order commensurate structure (such as one represented by $\cdot 4 \cdot 5$) or has no repeat period and is *incommensurate*.

In a number of cases the magnetic wavevector q_m, which typically varies with temperature, may hold to particular values in various temperature intervals. These values correspond to commensurate structures [7, 8, 30], and this 'lock-in' behaviour indicates that such structures represent energy minima in these systems. In the example of Er introduced in section 1.1 the lock-in wavevectors occur in the phase with cycloidal order; the lowest symmetry of the perturbing field is twofold, along the inversion axis of the HCP lattice. With $f = 2$, equation (10) gives $k = 4$, and we find from (11) that the lock-in values of $\frac{1}{4}$, $\frac{6}{23}$, $\frac{5}{19}$, $\frac{4}{15}$, and $\frac{2}{7}c^*$ give the corresponding spin-slip structures of commensurate, $\cdot 5$, $\cdot 4$, $\cdot 3$, $\cdot 2$, and $\cdot 1$ [8]†.

With this in mind consider $Ho_{0.5}Er_{0.5}$ in the low-temperature conical-spiral phase. We observe that q_m locks into a value of $0.225c^*$, or $9/40c^*$. In the undistorted lattice the basal-plane symmetry would be sixfold and, by (10), $k = 2$. This gives $x_s = 20/7$, which is not an integer, and the lock-in value of q_m would not correspond to a commensurate structure. Yet with the lattice distortion the sixfold symmetry may be broken. In the cases where the symmetry is reduced to either threefold or onefold we obtain $kf = 9$, and subsequently $x_s = 80$. Both cases correspond to low-order commensurate structures specified by $\cdot 26$ with $k = 3$, or $\cdot 8$ with $k = 9$.

The latter case with $k = 9$ is attractive for two reasons. First, it allows a direct correspondence between the lattice distortion of 8–9 planes between lattice slips and the sizes of the blocks of the magnetic structure. The lattice distortion 'separates' the blocks, thereby freezing in the local structure. Second, a sawtooth-wave distortion propagating perpendicular to the basal planes has itself a onefold symmetry. It is noteworthy that in these cases the number of layers between spin-slips x_s is quite large.

† To be precise, the full period of the structure is denoted by a sequence of $\cdot p$ repeated enough times to bring the phase of the individual blocks to coalescence with the beginning of a $\cdot p$ unit. For example, the $\frac{2}{7}$ structure is completely specified by $\cdot 1$, but the $\frac{3}{11}$ structure is denoted $\cdot 2 \cdot 2$.

2.3.2. Anomalous energy and polarization dependence in the resonant satellites. At the lowest temperature of our measurements the intensity of the resonant satellites along the [001] direction show an unusual energy dependence. Figure 5 shows the peak-intensity of the $(0, 0, 4 - q)$ satellite as a function of incident energy for two different temperatures (above and below T_C) and for two different polarizations.

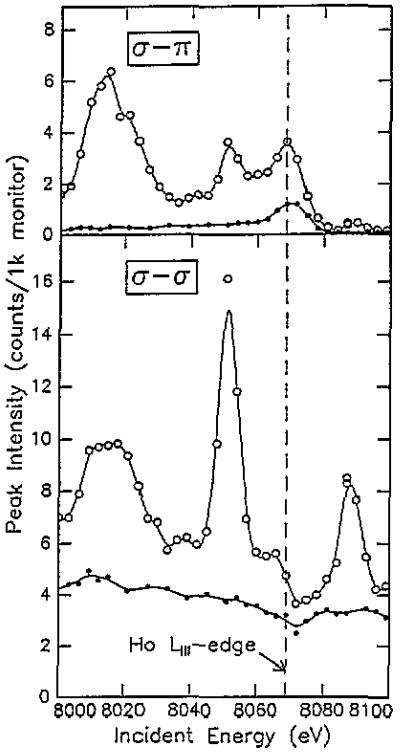

Figure 5. Intensity of the $(0, 0, 4-q)$ resonant satellite as a function of incident energy collected for two orthogonal polarizations. The lines are guides to the eye. Open circles (○) are for $T = 12$ K and closed circles (●) are for $T = 40$ K ($T_C = 35$ K).

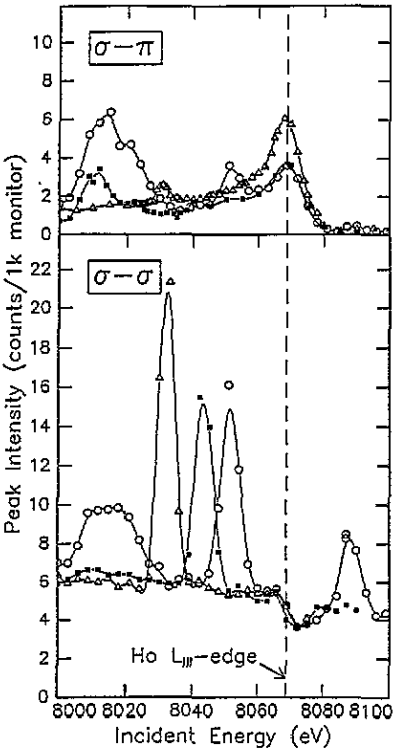

Figure 6. Intensity of the $(0, 0, 4-q)$ resonant satellite as a function of incident energy collected for two orthogonal polarizations at $T = 12$ K. The lines are guides to the eye. The open circles (○) are for data collected with the scattering plane oriented along the [100] direction of the crystal. The full boxes (■) are for the crystal rotated about the scattering vector by 7°relative to the scattering plane, and the open triangles (△) are for a rotation of 15°.

At 40 K the signals measured are typical of those which have been measured for pure Ho [14, 21]. The $\sigma \rightarrow \pi$ intensity increases strongly in the vicinity of the absorption edge, as the exchange interaction resonance comes into play at this point. At 12 K the resonance at the absorption edge remains, but there is significant additional intensity at three new energies: a peak of about 20 eV width at 8015 eV, a peak of about 10 eV width at 8051 eV, and a peak of about 7 eV width at 8087 eV. This anomalous signal is seen in both the $\sigma \rightarrow \pi$ and $\sigma \rightarrow \sigma$ channels.

Figure 6 repeats the 12 K scans under a rotation of the sample about the c axis by 7° and 15° measured from the [100] direction. We find that the peak at 8015 eV in the $\sigma \rightarrow \pi$ signal decreases and then disappears as the angle is changed. The peak at 8051 eV

in the $\sigma \rightarrow \sigma$ signal does not lose intensity, but shifts location to 8043 eV at 7° and then to 8038 eV at 15° rotation. The highest-energy peak at 8087 eV vanishes from the $\sigma \rightarrow \sigma$ intensity at 7° rotation.

The variation in intensity with such a rotation would suggest that the additional intensity is due to multiple scattering, which may occur whenever a pair of allowed reciprocal-space vectors combine to satisfy the scattering geometry at a particular energy. Given the evidence for a low-temperature lattice modulation, it is reasonable to suppose that such multiple scattering events would involve lattice-modulation (charge) satellites. Yet, as we show below, a careful treatment of the geometry of multiple scattering reveals that this mechanism is insufficient to explain this data, in spite of its qualitative appeal.

2.3.3. Multiple scattering. As is shown in figure 7, the geometrical condition for a multiple scattering event occurs when at least two points in the reciprocal lattice, say the scattering vector Q and κ, lie on the Ewald sphere [31]. The incoming radiation, which may scatter to all points of the sphere, scatters strongly to the extra point at κ. Then, this radiation may scatter through the vector κ' to Q and alter the intensity of the signal measured there. By rotating the crystal about Q the point κ will move off of the Ewald sphere, and the measured intensity will change. Further, depending on the particular κ involved in the process, such a rotation may cause the extra intensity to be picked up at a different incident energy, as the three relevant points (the origin **O**, Q and κ) now lie on a sphere of a different radius.

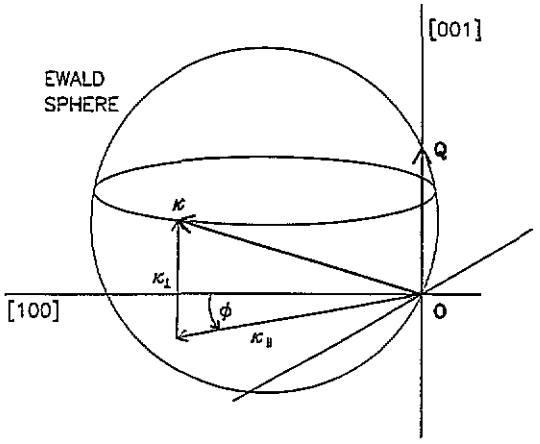

Figure 7. Illustration of the multiple-scattering geometry used to define the vector quantities discussed in the text.

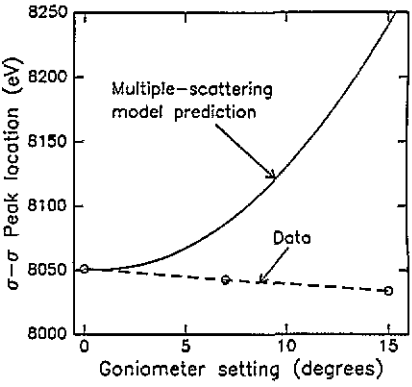

Figure 8. Comparison of the multiple scattering prediction and the location of the tallest anomalous peak in the $\sigma \rightarrow \sigma$ channel (shown in figure 6).

If we parametrize Q by $(0, 0, Q)$ and κ by $(\kappa_\parallel \cos\phi, \kappa_\parallel \sin\phi, \kappa_\perp)$, then the energy of the Ewald sphere which intersects these vectors and whose centre lies in the scattering plane is given by

$$E(\kappa, Q) = \hbar c[((\kappa^2 - Q\kappa_\perp)/2\kappa_\parallel \cos\phi)^2 + \tfrac{1}{4}Q^2]^{1/2} \tag{12}$$

where $\hbar c$ converts reciprocal-space units to energy units.

In the case of the anomalous peak at 8051 eV we know E as a function of the change in ϕ, so it is useful to write the derivative $dE/d\phi$ in terms of the known quantities E and Q:

$$dE/d\phi = E[1 - (Q\hbar c/2E)^2] \tan\phi. \tag{13}$$

The change in energy of the anomalous $\sigma \rightarrow \sigma$ peak is nearly linear with a slope of $-1.26\,\text{eV}$ per degree. At $E = 8051\,\text{eV}$ and $Q = 3.77c^* = 4.22\,\text{Å}^{-1}$, the solution to (13) gives $\phi = 0.7°$: κ would lie nearly in the scattering plane. We may carry the argument a bit further and note that because (13) contains only E, ϕ, and known constants, all subsequent derivatives of E contain only these terms as well; hence, we may develop an expression for $E(\phi)$ by means of a Taylor series expansion about $\phi_0 = 0.7°$ which is independent of the length of κ. This means that *any* vector κ which intercepts a set of energy spheres with particular E and particular $\mathrm{d}E/\mathrm{d}\phi$ must lie on a single $E(\phi)$ curve. This curve is shown in figure 8 by the full curve. Also pictured is the location of the anomalous $\sigma \rightarrow \sigma$ peak for the three different azimuths. It is quite clear that the multiple scattering model fails to account for the behaviour of this peak. We emphasize that this analysis depends only on energy conservation, and the assumption that the anomalous peak is due to double scattering from a single point in reciprocal space. Consequently, we may also rule out multiple scattering from a previously unknown element in reciprocal space, such as a reflection generated by twin formation.

With regard to the peak at 8015 eV, even though it does not follow the same azimuthal dependence as the peak discussed above, other reasons make multiple scattering an unlikely mechanism to explain its presence. First, to give sufficient intensity one of the reciprocal-space vectors should be a principal-lattice vector and the other should be a charge-scattering satellite, as the multiple scattering process is much weaker than the single-scattering process. Consequently, most intensity would be seen in the $\sigma \rightarrow \sigma$ polarization channel; any signal seen in the $\sigma \rightarrow \pi$ channel would come from spill-over due to imperfect polarization of the incident beam and imperfect filtering of the analyser. The degree of linear polarization in the incident beam P, defined as [7, 18]

$$P = (I_\sigma - I_\pi)/(I_\sigma + I_\pi) \tag{14}$$

is measured to be 0.85. Because the intensity of charge scattering in the $\pi \rightarrow \pi$ channel is proportional to $\cos^2(2\theta)$, where θ is the scattering angle, we find that this value for P gives the intensity of charge scattering due to π-incident radiation as approximately 2% of that due to σ-incident radiation. Yet at this energy the intensities are nearly equal in both the $\sigma \rightarrow \sigma$ and $\sigma \rightarrow \pi$ channels. Second, multiple magnetic scattering is also unlikely, as such a mechanism would be much weaker than single magnetic scattering; yet, as is evident in figure 5, the anomalous $\sigma \rightarrow \sigma$ peak at 8015 eV is of the same magnitude as the single-scattering peak at the absorption edge.

In spite of the failure of the multiple-scattering mechanism to account for the phenomenon the extra intensity must be due to scattering from the sample because the anomalous peaks vanish above T_C.

We believe that a successful explanation of the anomalous intensity measured from the satellites in the low-temperature phase must take into account the following features.

(i) The extra intensity is seen many tens of eV below the absorption edge. It is unlikely that the exchange interactions [13, 14] which give rise to an approximately 6 eV splitting seen in Ho between the E1 and E2 resonances can explain this much larger separation.

(ii) There is a weak azimuthal dependence in the anomalous signal. Crystal-field effects can give rise to a slow azimuthal variation in resonant scattering. Such a phenomenon has been observed in a study of the forbidden (111) reflection from haematite (α-Fe_2O_3) using a similar technique to that explored here [32]. The study found a sixfold variation in the resonant intensity as the crystal was rotated about the azimuthal angle; this was explained as the effect of the crystal field removing the degeneracy of the Fe 3d orbitals and splitting them into threefold symmetric bonding and antibonding states. Yet the energy

of the haematite resonance is precisely at the Fe K edge at 7112 eV, and no new resonant energies were reported.

(iii) The anomalous intensity has also been seen in a study of pure Er [33]. As in $Ho_{0.5}Er_{0.5}$ the anomalies in Er are seen only in the lowest-temperature phase, are accompanied by a lattice distortion, and have energies well below the principal resonance at the absorption edge.

Acknowledgments

We have benefited greatly from discussions with P Carra, D Gibbs, P Harris, B Lebech, P-A Lindgård, M Nielsen, A Sandy, and M K Sanyal. This work is supported in part from the Danish Natural Science Council.

References

[1] Koehler W C 1972 *Magnetic Properties of Rare Earth Metals* ed R J Elliott (New York: Plenum)
[2] Bozorth R M, Clark A E and Van Vleck J H 1972 *Int. J. Magnetism* **2** 19
[3] Cowley R A and Jensen J 1992 *J. Phys.: Condens. Matter* **4** 9673
[4] Cable J W, Wollan E O, Koehler W C and Wilkinson M K 1965 *Phys. Rev.* **140** A1896
[5] Koehler W C, Cable J W, Wilkinson M K and Wollan E O 1966 *Phys. Rev.* **151** 414
[6] Felcher G P, Lander G H, Arai T, Sinha S K and Spedding F H 1976 *Phys. Rev.* B **13** 3034
[7] Gibbs D, Moncton D E, D'Amico K L, Bohr J and Grier B H 1985 *Phys. Rev. Lett.* **55** 234
[8] Gibbs D, Bohr J, Axe J D, Moncton D E and D'Amico K L 1986 *Phys. Rev.* B **34** 8182
[9] Bohr J, Gibbs D, Moncton D E and D'Amico K L 1986 *Physica* A **140** 349
[10] Cowley R A and Bates S 1988 *J. Phys. C: Solid State Phys.* **21** 4113
[11] Shirane G and Pickart S J 1966 *J. Appl. Phys.* **37** 1032
[12] Howard B K and Bohr J 1991 *Phys. Scr.* T **39** 96
[13] Hannon J P, Trammell G T, Blume M and Gibbs D 1988 *Phys. Rev. Lett.* **61** 1245
[14] Gibbs D, Harshman D R, Isaacs E D, McWhan D B, Mills D and Vettier C 1988 *Phys. Rev. Lett.* **61** 1241
[15] Platzman P M and Tzoar N 1970 *Phys. Rev.* B **2** 3556
[16] Blume M 1985 *J. Appl. Phys.* **57** 3615
[17] Lovesey S W 1987 *J. Phys. C: Solid State Phys.* **20** 5625
[18] Blume M and Gibbs D 1988 *Phys. Rev.* B **37** 1779
[19] Carra P, Altarelli M and de Bergevin F 1989 *Phys. Rev.* B **40** 7324
[20] Lovesey S W 1993 *Rep. Prog. Phys.* 257
[21] Gibbs D, Grübel G, Harshman D R, Isaacs E D, McWhan D B, Mills D and Vettier C 1991 *Phys. Rev.* B **43** 5663
[22] Luo J, Trammel G T and Hannon J P 1993 *Phys. Rev. Lett.* **71** 287
[23] Hamrick M D 1991 *MA Thesis* Rice University
[24] Gibbs D, Blume M, Harshman D R and McWhan D B 1989 *Rev. Sci. Instrum.* **60** 1655
[25] Pearson W B 1964 *A Handbook of Lattice Spacings and Structures of Metals and Alloys* vol 1 (Oxford: Pergamon) p 125
[26] Feidenhans'l R 1989 *Surf. Sci. Rep.* **10** 105
[27] Helgeson G, Thurston T, Hill J P and Gibbs D 1993 *Bull. Am. Phys. Soc.* **38** 338
[28] Gibbs D 1993 private communication
[29] Overhauser A W 1971 *Phys. Rev.* B **3** 3173
Arfken G 1985 *Mathematical Methods for Physicists* (New York: Academic) pp 573–91
[30] Bohr J, Gibbs D and Huang K 1990 *Phys. Rev.* B **42** 4322
[31] Cole H, Chambers F W and Dunn H M 1962 *Acta Crystallogr.* **15** 138
[32] Finkelstein K D, Shen Q and Shastri S 1992 *Phys. Rev. Lett.* **69** 1612
[33] Sanyal M K, Gibbs L D, Bohr J and Wulff M 1994 *Phys. Rev.* B **49** 1079